https://doi.org/10.5194/essd-2026-233
Preprint. Discussion started: 8 May 2026

Open Access Earth System Science Data Discussions

An equidistant nodal orthogonal polynomial fitting model for the central Pacific Ocean basin derived from satellite altimeter data: eight major tidal harmonic constants

Deyu Meng[1,2], Yunfei Zhang[1,2], Yibo Zhang[3],Xiaojiang Zhang[3],Xianqing Lv[1,2]

[1]State Key Laboratory of Physical Oceanography, Ocean University of China, Qingdao, 266100, China
[2]Laboratory for Ocean Dynamics and Climate, Qingdao Marine Science and Technology Center, Qingdao, 266237, China
[3]College of Meteorology and Oceanography, National University of Defense Technology, Changsha, 410073, China

Correspondence to: Xiaojiang Zhang zhangxiaojiang19@nudt.edu.cn ; Xianqing Lv, xqinglv@ouc.edu.cn .

Abstract. High-precision tidal harmonic constants serves as an important foundation for numerical ocean tidal modeling and studies of tidal dynamics. Prior studies have validated the applicability and efficacy of the equidistant node orthogonal polynomial for the fitting of tidal harmonic constants. In this study, observational records acquired from the TOPEX/Poseidon, Jason-1, Jason-2, and Jason-3 satellite altimetry missions are employed to conduct a systematic tidal harmonic analysis over the Central Pacific Basin. The dataset generated by the Equidistant Node Orthogonal Polynomial Fitting (ENOPF) model for the Central Pacific Basin (170°E–230°W, 30°S–30°N) was used to construct cotidal charts for the eight major tidal constituents (M_2, S_2, N_2, K_2, K_1, O_1, P_1, Q_1). The dataset has a spatial resolution of 3′ × 3′, and its tidal amplitude and phase lags are quantitatively compared with outputs from the Finite Element Solutions 2014 (FES2014), FES2022b, Empirical Ocean Tide 20 (EOT20), Tidal Prediction eXtended OSU 10 (TPXO10), and Technical University of Denmark 16 (DTU16) tide models. The results show that, relative to the comparative models, the vector error (VE), mean absolute error of amplitude (ΔH), and mean absolute error of phase lag (ΔG) computed with satellite altimeter data and tide gauges exhibit superior performance using ENOPF dataset. For example, for the M_2, S_2, K_1, and O_1 tidal constituents, the vector errors between the ENOPF-derived dataset and data from satellite altimeters were 0.91, 0.44, 0.41, and 0.21 cm. Furthermore, the ENOPF method offers a simpler and faster method for improving resolution; subsequently, by extracting the polynomial coefficients, a more detailed dataset with resolution of 1′ × 1′ can be constructed. This high-precision tidal harmonic constant dataset for the Central Pacific Basin offers significant application advantages, providing more reliable data support and technical references for tidal dynamics, ocean circulation, and marine engineering projects in the region.

1 Introduction

Ocean tides represent a fundamental component of physical oceanographic research, with their dynamic behaviors and spatiotemporal variability exerting critical influences across diverse geophysical disciplines, including storm surge dynamics, sea level variability (Talke and Jay, 2020), crustal deformation, and large-scale ocean circulation (Green et al., 2009; Idier et

https://doi.org/10.5194/essd-2026-233
Preprint. Discussion started: 8 May 2026

al., 2019; Weber and Thomas, 2017). Comprehensive investigation of the eight primary astronomical tidal constituents—M_2, S_2, N_2, K_2, K_1, O_1, P_1, and Q_1—constitutes an indispensable basis for rigorous tidal harmonic analysis and predictive modeling. Furthermore, accurate characterization of these constituents provides essential support for practical applications spanning marine engineering (Mofjeld, 1988), navigational operations, coastal hazard mitigation, and marine ecosystem studies (Luneva et al., 2015).

The study region is located in the central Pacific Ocean, spanning the geographic domain bounded by 30°S–30°N and 170°E–130°W. The study area is dominated by the Central Pacific Basin, the northern sector of the South Pacific Basin, and the Tonga Trench, where seafloor topography evolves gradually from broad, gently sloping abyssal plains to subduction related deep sea trenches, characterized by pronounced topographic gradients (Hu et al., 2022). The maximum water depth within the domain reaches approximately 10,882 meters, corresponding to the deepest segment of the Tonga Trench. The Pacific Ocean covers nearly half of Earth's total oceanic area, and its complex and heterogeneous seafloor morphology—including mid ocean ridges, deep sea trenches, and island arc systems—together with its extensive, deep abyssal basins (Parianos and Madureira, 2021), provides a distinct physical environment for the generation, propagation, and energy dissipation of ocean tides. Therefore, obtaining high-precision tidal harmonics is of critical scientific importance for the study of tidal dynamics in the open ocean. Research on tidal charts for the central Pacific has a long history. Early studies completed the compilation of tidal charts for the four major tidal components—M_2, S_2, N_2, and K_1—in this region (Luther and Wunsch, 1975). Subsequently, with the widespread application of satellite altimetry data from satellites such as T/P and Jason, research on tidal harmonics has been systematically conducted across multiple regions of the Pacific, significantly improving the spatial accuracy and reliability of tidal charts for the Pacific Ocean (Niwa and Hibiya, 2001; Seifi et al., 2019; Yanagi et al., 1997).

Conventional investigations of ocean tides have historically depended upon water level observations acquired from coastal tide gauges (Stammer et al., 2014). Nevertheless, such measurements not only suffer from restricted spatial coverage but are only capable of resolving tidal characteristics within nearshore domains (Fu et al., 2025), which limits the effective characterization of tidal dynamical processes and their spatial distribution in the deep ocean (Fang et al., 2004). In contrast, satellite altimeter observations from the TOPEX/Poseidon mission have enabled a crucial advance in tidal science, revealing that the conversion of barotropic tidal energy to internal tidal motions—modulated by mid-ocean ridge topography—acts as a dominant mechanism for tidal dissipation in the deep ocean (Munk, 1997). This pivotal discovery, enabled directly by satellite altimetry, has fundamentally revised the longstanding paradigm in which tidal dissipation within the bottom boundary layers of marginal seas was regarded as the primary contributor. Furthermore, satellite altimetry measurements provide essential constraints for investigations of global sea surface dynamical processes and have notably improved the precision of tidal parameter estimation across the global ocean (Fang et al., 2004; Stammer et al., 2014). Consequently, satellite altimetry has become a fundamental data resource for the development and quantitative validation of tidal models (Hart-Davis et al., 2021). To date, a series of studies have confirmed that polynomial methods can be employed for the fitting of tidal harmonic constants; the fitted data can further be utilized to generate smooth cotidal charts (Wang et al., 2022; Xu et al., 2021; Zhang et al., 2023), and the resulting root mean square error (RMSE) values are found to be comparable in accuracy to those of mainstream global

https://doi.org/10.5194/essd-2026-233
Preprint. Discussion started: 8 May 2026

tidal models such as FES2014 and FES2022b. The equidistant node orthogonal polynomial fitting (ENOPF) method was first proposed by Eisinberg and Fedele (2007). Existing research has confirmed that the ENOPF method can be effectively employed for the fitting of tidal harmonic constant data (Zhang et al., 2023; Zhang et al., 2024; Zhang et al., 2025; Zhang et al., 2026). This method offers superior computational efficiency and is of significant importance to research on tidal dynamics. This approach is broadly applicable across global open ocean domains and furnishes high-accuracy open boundary conditions for coastal regional tide modeling. These remarkable advantages provide strong support for the use of the ENOPF method as a reliable solution in tidal modeling and coastal ocean dynamics research.

To improve the capability of deriving high-precision tidal harmonic constants in the central Pacific Ocean, this study utilizes observations from the T/P-Jason satellite altimeter and applies the ENOPF method. First, 3′ × 3′ tidal harmonic constants dataset and cotidal charts are generated; then, by extracting polynomial coefficients, high-resolution 1′ × 1′ tidal harmonic constants dataset are constructed. This high-precision tidal harmonics dataset for the Central Pacific Basin offers significant application advantages, providing more reliable data support and technical references for tidal dynamics, ocean circulation, and marine engineering projects in the region (Niwa and Hibiya, 2001; Ray and Cartwright, 2001; Kawasaki et al., 2021).

In this study, the FES2014 model with a horizontal resolution of 1/16°, FES2022b model with a horizontal resolution of 1/30°, TPX10 model with a horizontal resolution of 1/30°, EOT20 model with a horizontal resolution of 1/8°, and DTU16 model with a horizontal resolution of 1/16°are selected (as listed in **Table 1**), and their results are compared and analyzed with those derived from the equidistant node orthogonal polynomial fitting method.

The remainder of the paper is structured as follows: Section 2 systematically describes the datasets and core research methods employed in this study. Section 3 verifies the reliability of the dataset obtained by the ENOPF method in the Central Pacific Basin region through cross-comparison with results from classical tidal models, and presents cotidal charts for the eight major tidal constituents (M_2, S_2, K_1, O_1, N_2, K_2, P_1, and Q_1) in this region. Finally, Section 4 provides a comprehensive summary of the entire paper.

https://doi.org/10.5194/essd-2026-233
Preprint. Discussion started: 8 May 2026

Table 1. Details of the model data

Tide models	Resolution	Type	Reference
FES2014	1/16°	assimilation model	(Lyard et al., 2021)
FES2022b	1/30°	assimilation model	(Carrere et al., 2022)
TPXO10	1/30°	assimilation model	(Egbert and Erofeeva, 2002)
EOT20	1/8°	empirical model	(Hart-Davis et al., 2021)
DTU16	1/16°	empirical model	(Cheng and Andersen, 2011)

2 Data and Methods

2.1 Data

2.1.1 Satellite Altimeter

The study area is part of the central Pacific (30° S–30° N, 170° E–130° W). The satellite altimeter data employed in this study covers the period from October 1992 to September 2017, spanning 25 years, which is far longer than the aliasing periods of the eight major tidal constituents; consequently, these satellite altimetry data can be effectively used for tidal harmonic analysis. The satellite altimeter data used include observations from the TOPEX/Poseidon (T/P) satellite (August 1992–December 2001), Jason-1 satellite (December 2001–June 2008), Jason-2 satellite (June 2008–January 2016), and Jason-3 satellite (January 2016–September 2017). All of the aforementioned satellites operated on the same orbit, with a sampling period of 9.9156 days. Satellite altimeter observations in open ocean regions are generally of high quality, but preprocessing is still required to ensure data accuracy. To obtain the highest-precision sea surface height data, this study preprocessed the raw satellite altimeter data using Geophysical Data Records (GDR) in accordance with the OSTM/Jason-2 product manual. The sea surface height values relative to the solid Earth surface, as measured by the satellite altimeter, are given by the following Eq. (1):

$$h = Sea\ surface\ height - Mean\ surface - Solid\ Earth\ tide\ height - Load\ tide - Pole\ tide\ height - Inverted\ barometer\ height\ correct - High\ frequency\ fluctuations\ of\ sea\ surface\ topography \quad (1)$$

2.1.2 Tide Gauge

The tide gauge data employed in this paper were obtained from the University of Hawaii Sea Level Center (UHSLC). Water level data from 13 tide gauges were selected for tidal harmonic analysis, and the derived results were compared with those obtained via the ENOPF method to calculate the vector error.

https://doi.org/10.5194/essd-2026-233
Preprint. Discussion started: 8 May 2026

Open Access Earth System Science Data Discussions

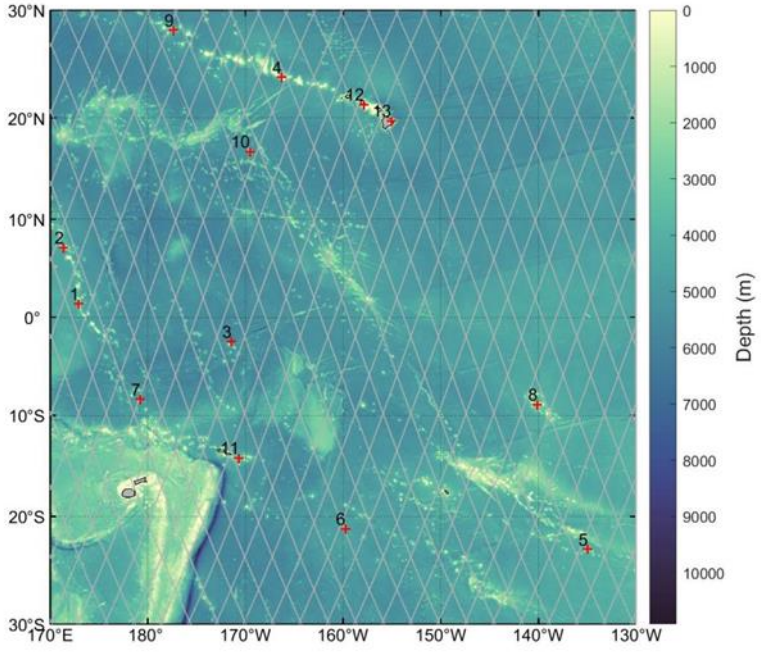

110 **Figure 1.** Bathymetry (m) surrounding the central Pacific Ocean basin. The 13 tidal gauges are denoted by red plus signs (as listed in **Table 2**). The gray lines indicate the satellite tracks.

Table 2. Detailed information of 13 tidal gauges.

Number	Station	Longitude (°)	Latitude (°)
1	Tarawa, Gilbert Is	172.93	1.362
2	Majuro	171.367	7.1
3	Kanton Is., Phoenix Is	188.57	-2.49
4	French Frigate Shoals, H	193.717	23.866
5	Rikitea, Gambier	225.05	-23.133
6	Rarotonga	200.233	-21.2
7	Funafuti, Ellice Is	179.217	-8.383
8	Nuku Hiva, Marquesas Is	219.917	-8.933
9	Midway Is, Hawaiian Is	182.633	28.217
10	Johnston	190.467	16.733
11	Pago Pago, American Samoa	189.317	-14.283
12	Honolulu, Hawaiian Is	202.133	21.3
13	Hilo, Hawaiian Is	204.933	19.733

https://doi.org/10.5194/essd-2026-233
Preprint. Discussion started: 8 May 2026

Open Access Earth System Science Data Discussions

2.2 Method

2.2.1 Tidal harmonic analysis

Based on the least squares method, water level is treated as a linear superposition of a series of cosine functions (as Eq.(2)). Tidal harmonic analysis (Doodson, 1924) is conducted on the sea surface height data from satellite altimeters and water level data from tide gauges (Foreman and Henry, 1989; Pawlowicz et al., 2002) within the study area, thereby determining the tidal harmonic constants of the eight major tidal constituents (M_2, S_2, N_2, K_2, K_1, O_1, P_1, and Q_1) — namely, the amplitudes and phase lags corresponding to each cosine function are derived (Zetler et al., 1965).

$$h(t) = A_0 + \sum_j A_j \cos(\sigma_j t - \theta_j) \tag{2}$$

where A_0 denotes the mean sea level at a given data point used for harmonic analysis, and A_j, σ_j, and θ_j represent the amplitude, frequency, and phase lag of the *j*-th tidal constituent, respectively. The term $h(t)$ includes sea surface height variations induced by non-tidal and residual "noise" contributions.

2.2.2 Equidistant nodal orthogonal polynomial fitting

In this study, the equidistant node orthogonal polynomial fitting method is employed to fit satellite altimeter data. The ENOPF method was proposed (Eisinberg and Fedele, 2007), and has been proven to be effective for fitting tidal harmonic constants. Direct fitting of amplitude and phase complicates the fitting process, mainly due to the following reasons: the periodicity of phase tends to cause numerical discontinuity, the coupling characteristics of amplitude and phase require more complex optimization algorithms for nonlinear fitting (Zhang et al., 2025), and phase fitting is sensitive to noise, making it difficult to ensure accuracy. Therefore, to avoid the complex calculation of fitting phase lags, the amplitude *H* and phase lag *G* are transformed in this study to obtain $a=H\,cosG$ and $b=H\,sinG$. The ENOPF method is then used to fit *a* and *b*, where *H* denotes the amplitude and *G* represents the phase lag derived from harmonic analysis. After obtaining the values of a and b through fitting, the amplitude *H* and phase lag *G* are derived inversely using Eq. (3) and (4).

$$H = \sqrt{a^2 + b^2} \tag{3}$$

$$G = arctan(a/b) \tag{4}$$

First, the longitude and latitude grid points are normalized, and the longitude and latitude coordinates of each satellite subsatellite point are transformed onto the regular grid points *x* and *y*, thereby enabling the reasonable use of orthogonal polynomials as basis functions and further improving the calculation accuracy.

Assuming there are *k* equidistant nodes with the same step size in the one-dimensional direction, and setting the weight function $\omega_i = 1$, the following transformation exists: $x=1, 2, \ldots k$. Then a one-dimensional equidistant node *m-th* order polynomial in the *x*-direction was constructed (Eq. (5)), where m denotes the order of the polynomial in the *x*-direction.

$$\Phi_0(x) = 1$$

$$\Phi_1(x) = x - \frac{1}{2}(k+1)$$

$$\Phi_{m+1}(x) = \Phi_1(x)\Phi_m(x) - \frac{m^2(k^2-m^2)}{4(4m^2-1)}\Phi_{m-1}(x) \tag{5}$$

https://doi.org/10.5194/essd-2026-233
Preprint. Discussion started: 8 May 2026

Within the domain of definition, the following relationship exists:

$$\sum_{x=1}^{k} \Phi_i(x)\Phi_j(x) = 0;\ i \neq j \tag{6}$$

where $i=0,1,2,\ldots,m-1$ and $j=0,1,2,\ldots,n-1$, with n denoting the order of the polynomial in the y-direction.

In the two-dimensional direction, the expression of the equidistant node orthogonal polynomial is:

$$D(x,y) = \sum_{i=0}^{m}\sum_{j=0}^{n} B_{i,j}\,\Phi_i(x)\Psi_j(y) \tag{7}$$

Where $B_{i,j}$ denotes the polynomial coefficient of degrees i and j, which can be calculated by the least squares method; $\Psi_j(y)$ is the expression of the equidistant node orthogonal polynomial in the y-direction, and $\Phi_i(x)$ is the expression of the equidistant node orthogonal polynomial in the x-direction.

From the definition of the equidistant node orthogonal polynomial, the following relationship exists:

$$\begin{aligned} &\sum_{i=1}^{N} \phi_k(x_i)\phi_m(x_i) = 0, k \neq m, \\ &\sum_{i=1}^{N} \psi_s(y_i)\psi_n(y_i) = 0, s \neq n, \end{aligned} \tag{8}$$

2.2.3 Cross-validation

In this study, the fitting order of the Equidistant Node Orthogonal Polynomial serves as a critical parameter influencing fitting accuracy and numerical stability (Zhang et al., 2024), which requires rational selection in conjunction with data characteristics and physical processes. On one hand, an excessively low fitting order will lead to model "underfitting," making it difficult to capture the spatial variation details of harmonic constants such as amplitude and phase within the study area. On the other hand, an excessively high fitting order may induce the problem of "overfitting," resulting in physically meaningless spatial jumps in the gridded harmonic constants (e.g., phase mutations, abnormal amplitude fluctuations) that violate the continuous variation laws of ocean/atmospheric waves. Additionally, an excessively high order will increase computational complexity and reduce fitting efficiency. Therefore, this study determines the optimal fitting order through the cross-validation method: with the goal of minimizing the sum of squared fitting residuals, iterative calculations are performed step-by-step within the range of 2–11 order polynomials.

Specifically, the existing data samples are randomly divided into 10 subsets. One subset is selected as the validation set, and the remaining nine subsets serve as the training set. The orders of the polynomial in the zonal (east-west) and meridional (north-south) directions within the training set are adjusted to obtain training set results corresponding to different directional orders. Subsequently, the validation set data are imported into these models respectively to derive and record the vector errors of the fitting results for different order combinations. The above cross-validation process is repeated 10 times in total to determine the vector errors corresponding to each order combination. By comparing the vector errors of different order combinations, the optimal order combination is identified (as listed in **Table 3**).

Table 3. The optimal orders of ENOPF for the eight tidal constituents

	M_2	S_2	K_1	O_1	N_2	K_2	P_1	Q_1
m	5	4	5	4	4	4	5	4
n	4	5	4	5	5	5	4	5

https://doi.org/10.5194/essd-2026-233
Preprint. Discussion started: 8 May 2026

Open Access Earth System Science Data Discussions

3 Results and Discussion

3.1 Comparison of the fit results and orbital data

In this study, the dataset derived from the Equidistant Node Orthogonal Polynomial Fitting (ENOPF) method, the results of five other models, and the along-track data are compared. The comparison metrics include Vector Error (*VE*), mean absolute error of amplitude (ΔH), and mean absolute error of phase lag (ΔG), with the calculation methods as follows Eq. (9), (10), and (11):

$$VE = \left[\frac{1}{2}(H_e^2 + H_o^2) - H_e H_o \cos(G_e - G_o)\right]^{1/2} \quad (9)$$

$$\Delta H = |H_e - H_o| \quad (10)$$

$$\Delta G = |G_e - G_o| \quad (11)$$

where *e* and *o* represent the results of each model experiment and the satellite altimeter observation data, respectively.

Through comparisons of the dataset derived from the ENOPF method, the outputs of five other tidal models, and satellite altimeter data (as listed in **Table 4**), it is evident that the Vector Error (*VE*), mean absolute error of amplitude (ΔH), and mean absolute error of phase lag (ΔG) derived from the ENOPF method for the M_2, S_2, K_1, N_2, K_2 and P_1 are consistently smaller than those obtained from the other models. For the O_1 constituent, the mean absolute error of phase lag (ΔG) from the ENOPF dataset is slightly larger than that of the TPXO10 and DTU16 models; however, the ENOPF dataset yields the smallest values for both the mean absolute error of amplitude (ΔH) and vector error (*VE*) across all models. Regarding the Q_1 constituent, the mean absolute error of phase lag (ΔG) from the ENOPF dataset is smaller than that of the other five models, while the mean absolute error of amplitude (ΔH) and vector error (*VE*) values are nearly equivalent among all compared models.

https://doi.org/10.5194/essd-2026-233
Preprint. Discussion started: 8 May 2026

Open Access Earth System Science Data Discussions

Table 4. The errors of the ENOPF method and the five models for the eight major tidal constituents compared to the satellite altimeter data.

		ENOPF	FES2014	FES2022b	EOT20	TPXO10	DTU16
M_2	$\Delta H(cm)$	0.81	2.57	2.56	2.59	2.44	2.50
	$\Delta G(deg)$	2.01	2.75	3.02	3.65	2.55	2.49
	$VE(cm)$	**0.91**	1.90	1.88	1.95	1.79	1.84
S_2	ΔH	0.43	0.82	0.75	0.95	0.77	0.71
	ΔG	2.88	4.00	3.90	5.38	4.00	4.29
	VE	**0.44**	0.64	0.60	0.77	0.62	0.57
K_1	ΔH	0.37	0.93	0.95	0.97	0.80	0.75
	ΔG	5.22	8.63	8.65	8.81	8.28	8.56
	VE	**0.41**	0.78	0.79	0.82	0.68	0.66
O_1	ΔH	0.18	0.55	0.54	0.53	0.45	0.45
	ΔG	5.48	6.20	6.02	6.04	5.29	5.23
	VE	**0.21**	0.45	0.45	0.44	0.37	0.38
N_2	ΔH	0.26	0.56	0.56	0.59	0.55	0.56
	ΔG	3.20	6.49	6.37	7.03	6.49	6.55
	VE	**0.29**	0.46	0.45	0.48	0.45	0.46
K_2	ΔH	0.26	0.37	0.33	0.36	0.36	0.40
	ΔG	7.00	12.83	12.54	13.80	12.79	13.75
	VE	**0.29**	0.36	0.33	0.34	0.35	0.39
P_1	ΔH	0.27	0.38	0.39	0.39	0.34	0.40
	ΔG	10.79	20.14	20.14	20.24	20.28	20.38
	VE	**0.27**	0.37	0.38	0.38	0.34	0.39
Q_1	ΔH	0.22	0.23	0.23	0.22	0.23	0.22
	ΔG	20.40	38.62	37.64	38.97	38.40	26.57
	VE	**0.24**	0.26	0.26	0.26	0.26	0.26

https://doi.org/10.5194/essd-2026-233
Preprint. Discussion started: 8 May 2026

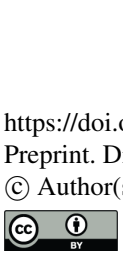

Open Access Earth System Science Data Discussions

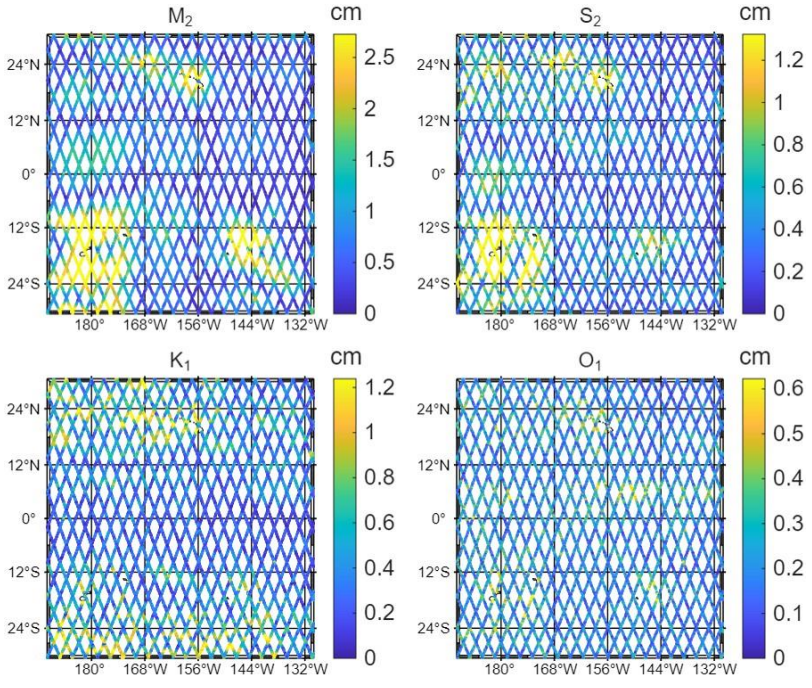

195

Figure 2. The distribution of vector errors of M_2, S_2, K_1, O_1 tidal constituents in the ENOPF dataset along the satellite orbit.

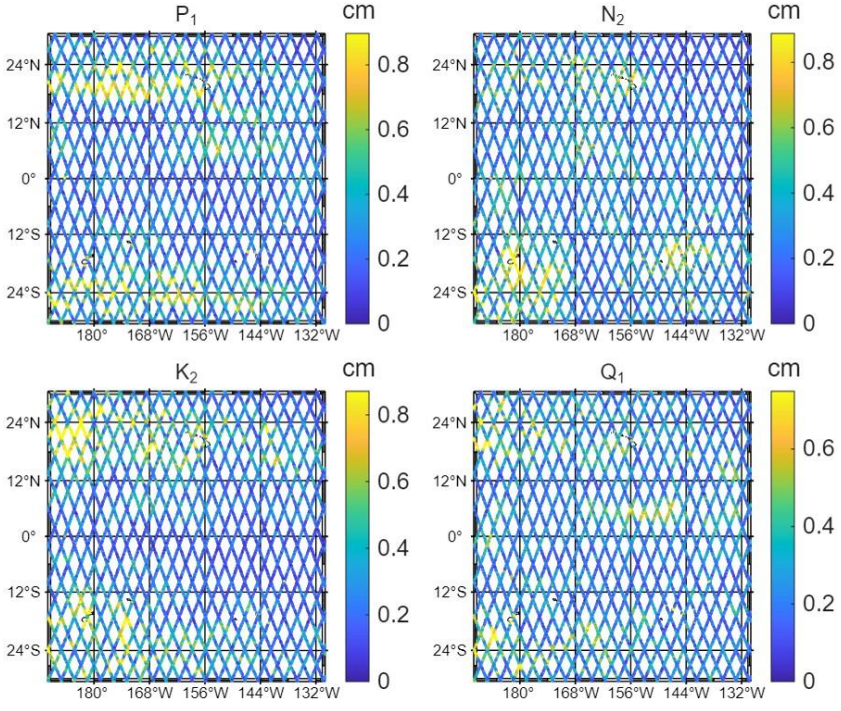

Figure 3. The distribution of vector errors of P_1, N_2, K_2, Q_1 tidal constituents in the ENOPF dataset along the satellite orbit.

https://doi.org/10.5194/essd-2026-233
Preprint. Discussion started: 8 May 2026

3.2 Compare the dataset with the tide gauge station data

Within the central Pacific Ocean (30°S–30°N, 170°E–130°W), water level data from 13 tide gauges were selected for tidal harmonic analysis. The derived amplitudes and phase lags were compared with the dataset derived from the ENOPF method and the outputs of five other tidal models, yielding the vector error (*VE*), mean absolute error of amplitude (*ΔH*), and mean absolute error of phase lag (*ΔG*).

Table 5. The errors of the dataset derived from the ENOPF method and the five models for the eight major tidal constituents compared to the tidal gauges.

		ENOPF	FES2014	FES2022b	EOT20	TPXO10	DTU16
M_2	*ΔH(cm)*	1.04	1.20	1.05	1.09	1.10	1.29
	ΔG(deg)	4.29	6.82	6.11	6.17	5.78	7.38
	VE(cm)	**2.04**	2.56	2.42	2.42	2.46	2.64
S_2	*ΔH*	0.70	0.86	0.74	0.90	0.77	0.99
	ΔG	5.67	6.92	8.67	7.05	6.16	8.18
	VE	**1.19**	1.31	1.29	1.34	1.22	1.40
K_1	*ΔH*	0.39	0.74	0.33	0.37	0.33	0.47
	ΔG	3.62	4.09	4.65	15.66	5.19	6.93
	VE	**0.36**	0.41	0.38	0.67	0.44	0.52
O_1	*ΔH*	0.15	0.12	0.21	0.26	0.18	0.30
	ΔG	4.69	5.08	3.39	4.88	6.39	5.01
	VE	**0.24**	0.30	0.29	0.33	0.30	0.31
N_2	*ΔH*	0.38	0.41	0.42	0.49	0.42	0.46
	ΔG	6.44	6.75	6.78	6.90	5.96	7.63
	VE	**0.57**	0.67	0.68	0.69	0.64	0.70
K_2	*ΔH*	0.26	0.48	0.27	0.36	0.24	0.34
	ΔG	9.87	8.32	3.01	11.55	6.43	7.97
	VE	0.37	0.39	0.38	0.49	**0.36**	0.42
P_1	*ΔH*	0.15	0.17	0.17	0.19	0.08	0.19
	ΔG	3.06	7.97	8.02	3.79	3.33	3.69
	VE	0.13	0.16	0.13	0.19	**0.10**	0.17
Q_1	*ΔH*	0.12	0.12	0.06	0.16	0.07	0.08
	ΔG	7.28	5.45	4.02	9.61	4.95	7.64
	VE	0.12	0.07	**0.07**	0.17	0.09	0.10

https://doi.org/10.5194/essd-2026-233
Preprint. Discussion started: 8 May 2026

Through comparative analysis, it is found that for the 13 tide gauges within the study region, the *VE*, *ΔH* and *ΔG* of the M_2 and S_2 tidal constituents derived from the ENOPF method are consistently smaller than those obtained from the other five models (as listed in **Table 5**). Although some models (e.g., FES2022b, EOT20, and TPXO10) yield slightly smaller mean absolute errors of amplitude (*ΔH*) for the K_1 and O_1 constituents compared to ENOPF-derived dataset, the ENOPF dataset exhibits the smallest vector error for the K_1 and O_1 constituents among all tested models. For the N_2 constituent, only the mean absolute error of phase lag (*ΔG*) from the TPXO10 model is smaller than that from the ENOPF dataset, while the ENOPF dataset outperforms all other models in the other two evaluation metrics (*VE* and *ΔH*). Regarding the K_2 and P_1 constituents, the performance of the ENOPF dataset is second only to that of the TPXO10 model. However, for the Q_1 constituent, the ENOPF method is superior only to the EOT20 model.

To more intuitively evaluate the vector difference results at each station, **Figure 4** illustrate the performance of different models for various tidal constituents at individual stations. Compared with models such as EOT20 and FES2022, this dataset achieves higher accuracy when validated against satellite altimetry and tide gauge observations. It optimizes the spatial representation of tidal harmonic constants across the Central Pacific Basin, and provides a robust data foundation for regional tidal dynamics and related oceanographic research.

https://doi.org/10.5194/essd-2026-233
Preprint. Discussion started: 8 May 2026

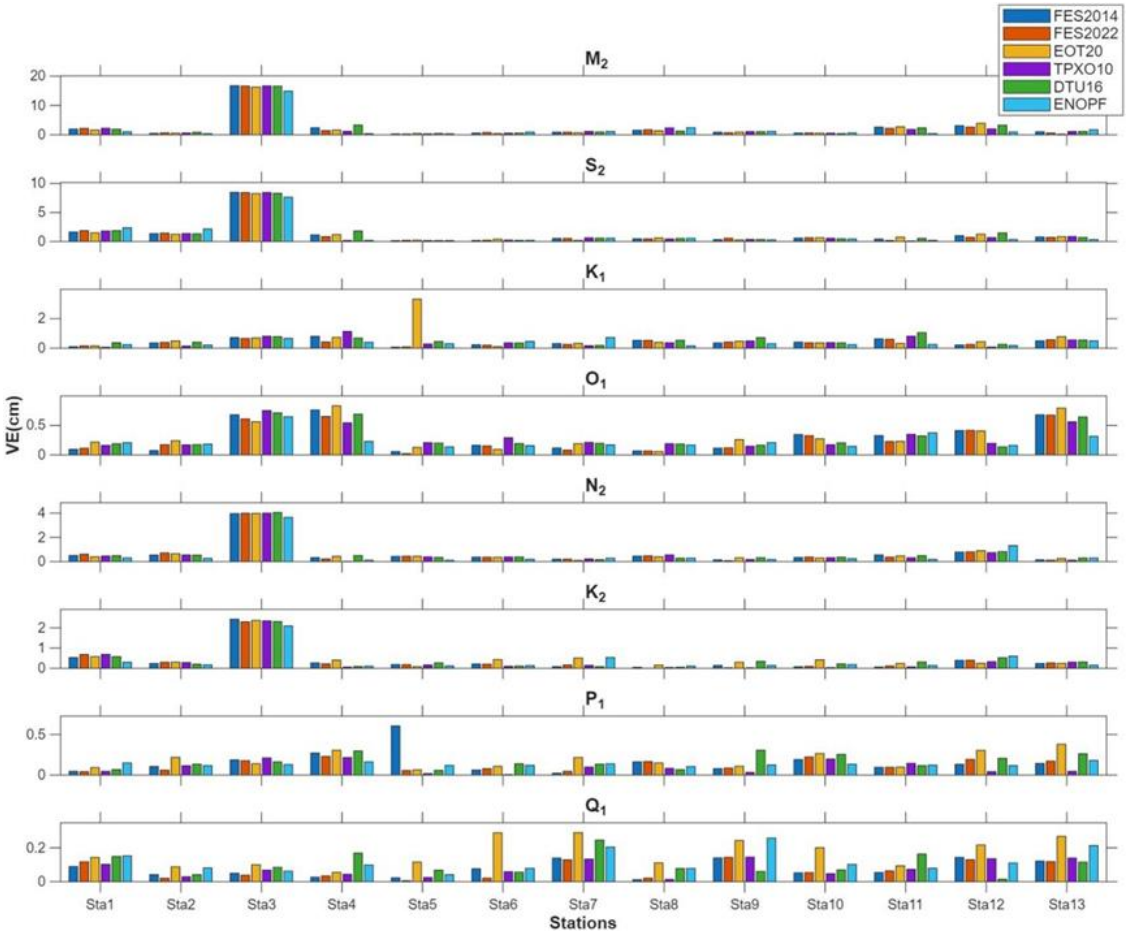

Figure 4. Distribution of vector errors in the ENOPF dataset and five models of eight major tidal constituents at 13 tide gauges.

225

3.3 Cotidal charts

The above evaluation data indicate that the harmonic constants dataset obtained by the ENOPF method within the study area are in good agreement with the tidal harmonic constants of the eight major tidal constituents derived from satellite altimetry data and tide gauges. In the following, this study presents the cotidal charts constructed based on the experimental results of
230 different models for the eight major tidal constituents (M_2, S_2, K_1, O_1, N_2, K_2, P_1, and Q_1).

https://doi.org/10.5194/essd-2026-233
Preprint. Discussion started: 8 May 2026

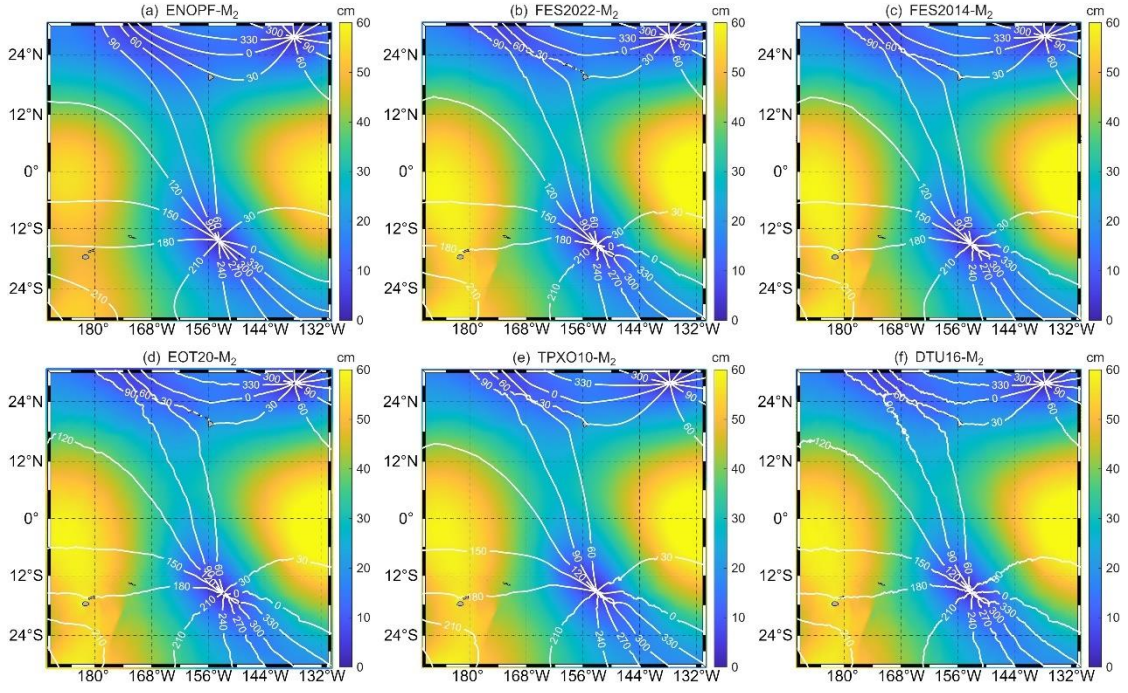

Figure 5. The cotidal charts of the M_2 tidal constituent for each model. (a) the ENOPF method, (b) the FES2022, (c) FES2014, (d) EOT20, (e) TPXO10 and (f) DTU16 models.

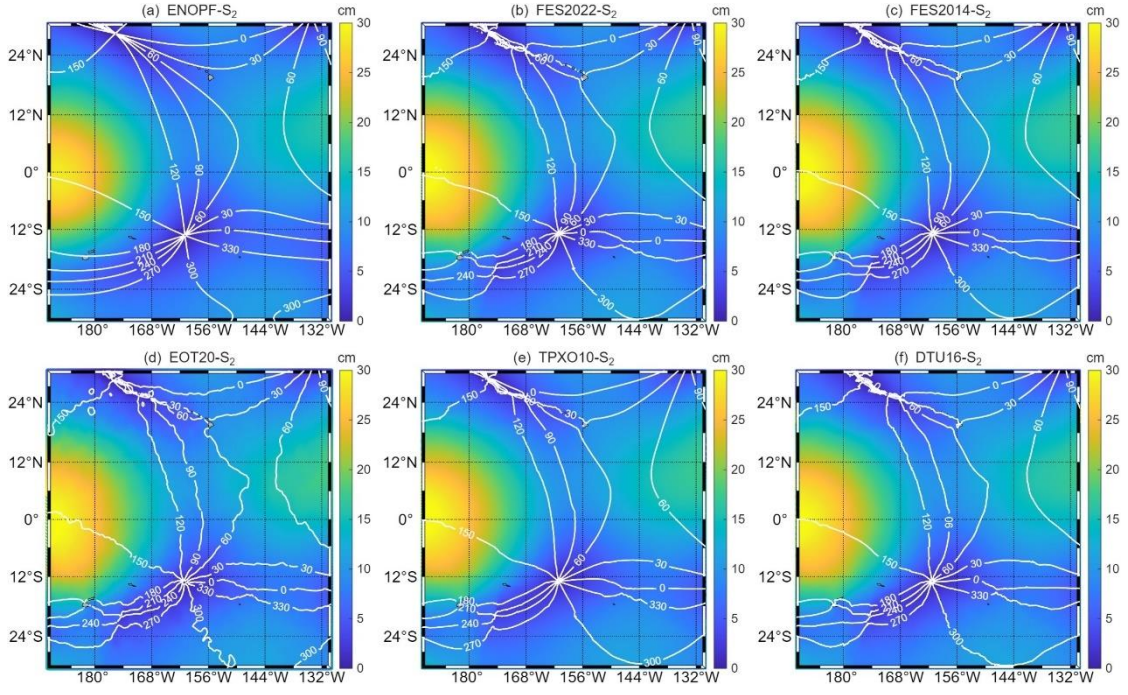

Figure 6. The cotidal charts of the S_2 tidal constituent for each model. (a) the ENOPF method, (b) the FES2022, (c) FES2014, (d) EOT20, (e) TPXO10 and (f) DTU16 models.

https://doi.org/10.5194/essd-2026-233
Preprint. Discussion started: 8 May 2026

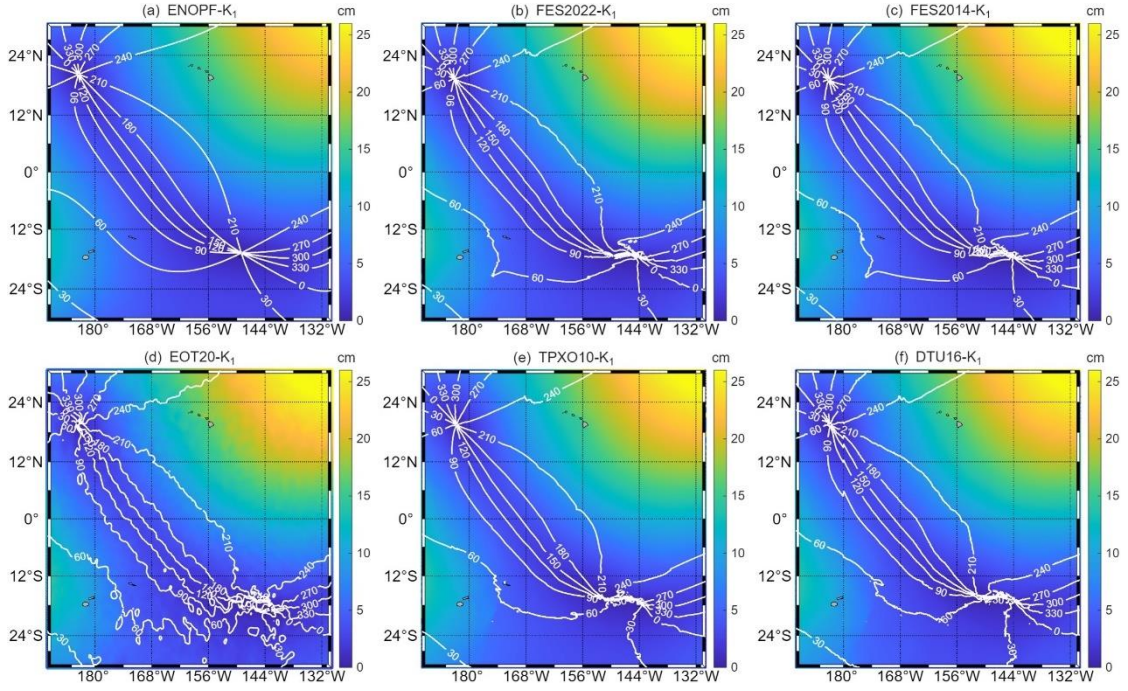

Figure 7. The cotidal charts of the K_1 tidal constituent for each model. (a) the ENOPF method, (b) the FES2022, (c) FES2014, (d) EOT20, (e) TPXO10 and (f) DTU16 models.

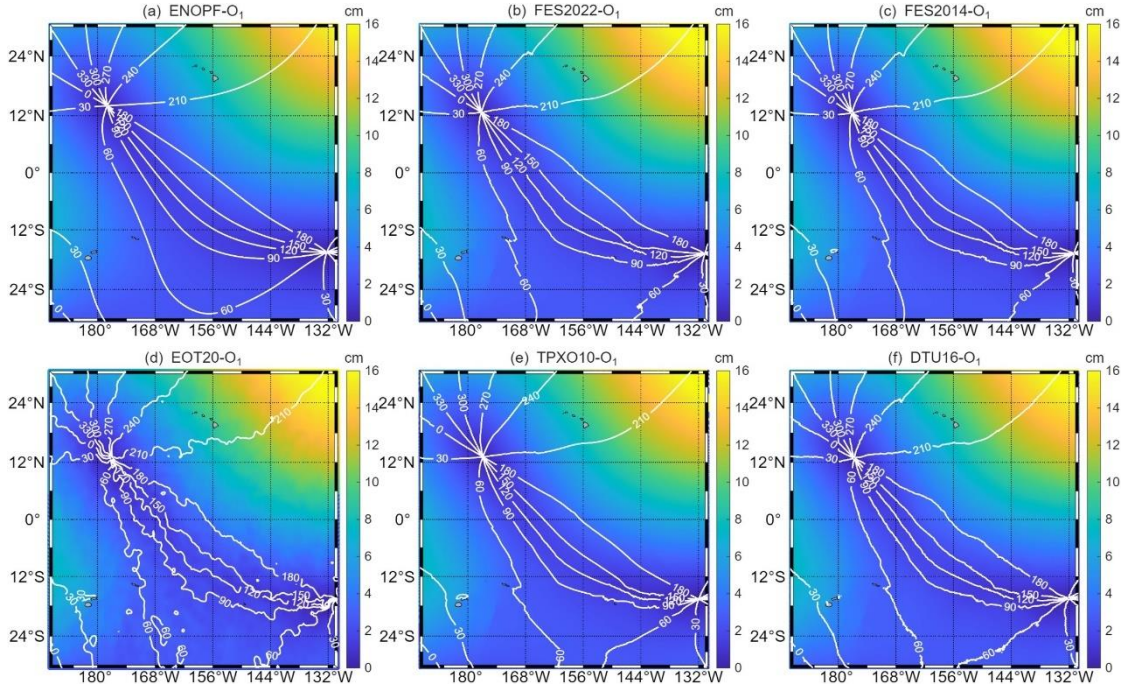

Figure 8. The cotidal charts of the O_1 tidal constituent for each model. (a) the ENOPF method, (b) the FES2022, (c) FES2014, (d) EOT20, (e) TPXO10 and (f) DTU16 models.

https://doi.org/10.5194/essd-2026-233
Preprint. Discussion started: 8 May 2026

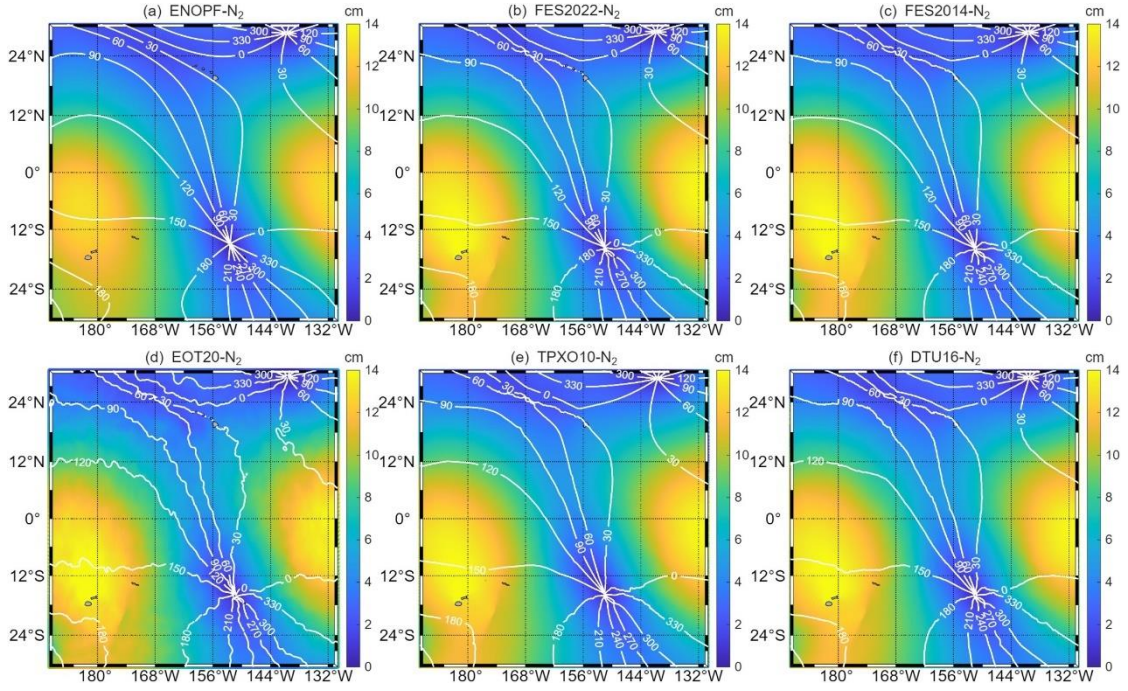

Figure 9. The cotidal charts of the N_2 tidal constituent for each model. (a) the ENOPF method, (b) the FES2022, (c) FES2014, (d) EOT20, (e) TPXO10 and (f) DTU16 models.

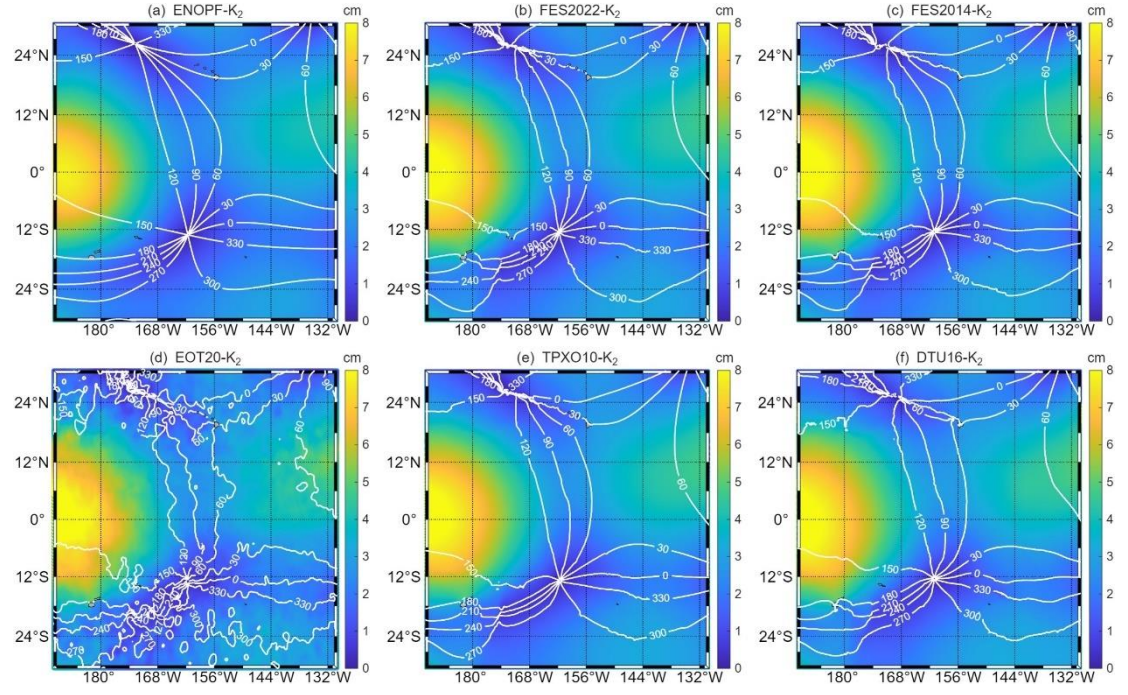

Figure 10. The cotidal charts of the K_2 tidal constituent for each model. (a) the ENOPF method, (b) the FES2022, (c) FES2014, (d) EOT20, (e) TPXO10 and (f) DTU16 models.

https://doi.org/10.5194/essd-2026-233
Preprint. Discussion started: 8 May 2026

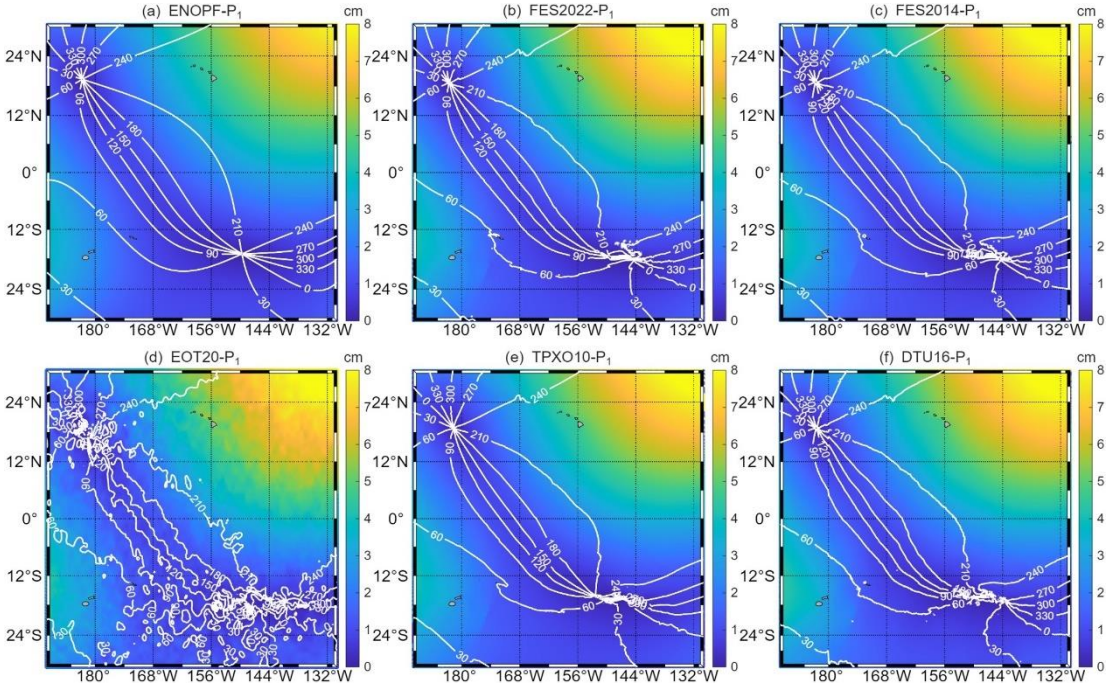

Figure 11. The cotidal charts of the P_1 tidal constituent for each model. (a) the ENOPF method, (b) the FES2022, (c) FES2014, (d) EOT20, (e) TPXO10 and (f) DTU16 models.

https://doi.org/10.5194/essd-2026-233
Preprint. Discussion started: 8 May 2026

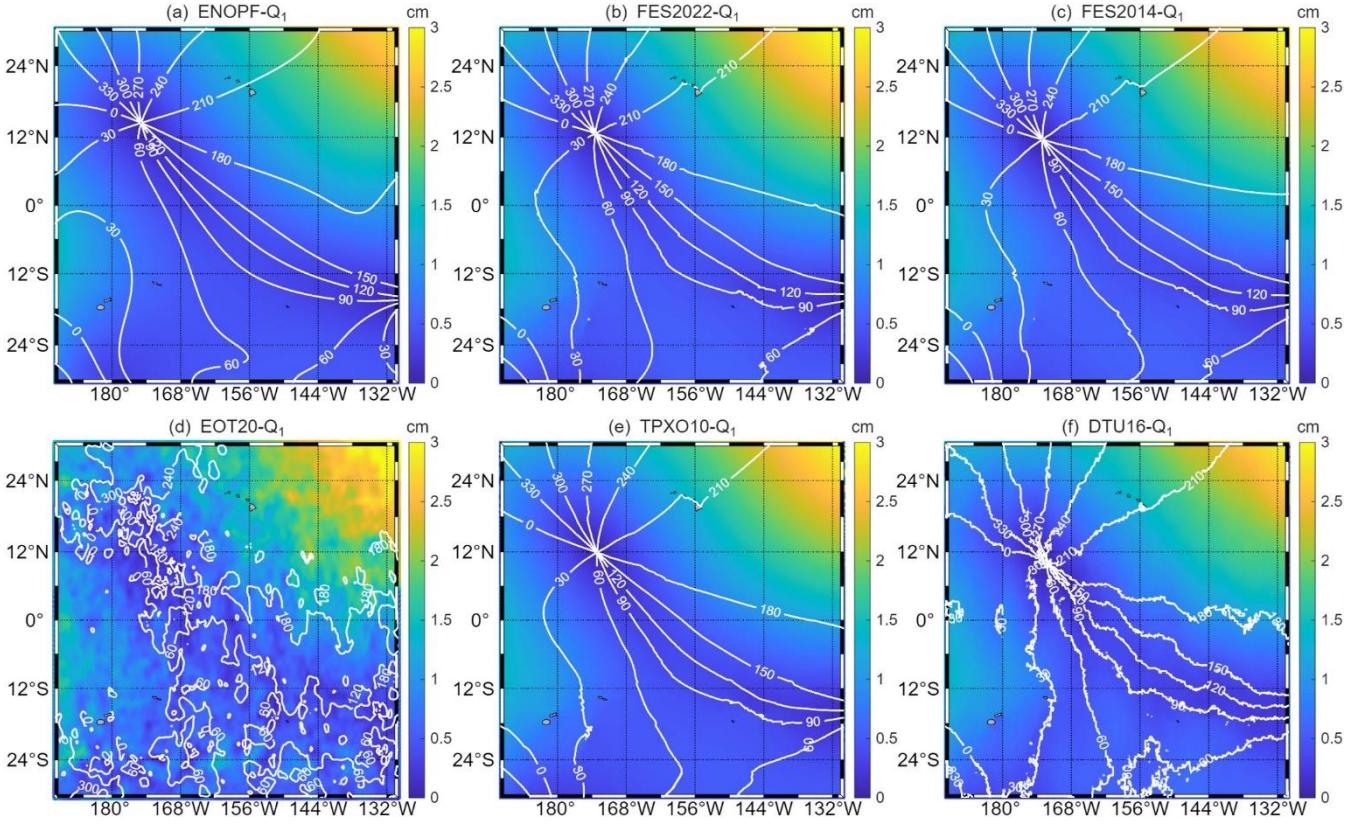

Figure 12. The cotidal charts of the Q_1 tidal constituent for each model. (a) the ENOPF method, (b) the FES2022, (c) FES2014, (d) EOT20, (e) TPXO10 and (f) DTU16 models.

A comparison of the cotidal charts derived from different datasets demonstrates that all models yield generally consistent simulations of the spatial distribution of tidal constituent amplitudes, the geographic positions of amphidromic points, and the trending of isophase lines. Specifically, the high-amplitude zones of diurnal tidal constituents are skewed toward the northeastern part of the study area, locating at the upper right of this region (**Fig. 7, 8, 11 and 12**); whereas the high-amplitude areas of semidiurnal tidal constituents are distributed along the eastern and western flanks of the study domain (**Fig. 5, 6, 9 and 10**). The isophase lines simulated by the EOT20 model exhibit a pronounced fragmented feature, which is clearly reflected in the EOT20 cotidal charts of the K_2, P_1 and Q_1 tidal constituents (**Fig. 10(d), 11(d) and 12(d)**). In contrast, the isophase lines (white curves) generated by the dataset of ENOPF show smooth and continuous convergent or divergent patterns, and the convergent morphology at the amphidromic points appears more regular.

https://doi.org/10.5194/essd-2026-233
Preprint. Discussion started: 8 May 2026

4 Conclusion

In this study, the dataset of tidal harmonic constants for eight major tidal constituents (M_2, S_2, N_2, K_2, K_1, O_1, P_1, Q_1) in the Central Pacific Basin (170°E–130°W, 30°S–30°N) was generated using the Equidistant Node Orthogonal Polynomial Fitting (ENOPF) method, with spatial resolutions of 3′×3′ and 1′×1′. The ENOPF method used to produce the dataset serves as a more valuable reference for the evaluation of tidal models, while providing high-precision boundary conditions for coastal tidal models. Furthermore, this method can be widely applied to tidal studies in the open ocean of the world's oceans.

The dataset with a spatial resolution of 3′×3′generated by the ENOPF method was compared with five tidal models (FES2014, FES2022b, TPXO10, EOT20, DTU16), using the mean absolute amplitude error (ΔH), mean absolute phase lag error (ΔG), and vector error (VE) as validation metrics. Evaluations were carried out against both satellite altimetry data and in-situ observations from 13 tide gauges. Results show that the ENOPF dataset achieves the smallest errors against satellite altimetry for most constituents (M_2, S_2, K_1, N_2, K_2, P_1). For the M_2 constituent, the three metrics reach 0.81 cm, 2.01°, and 0.91 cm, respectively, indicating a clear advantage over other models. When validated against tide gauge data, ENOPF exhibits lower vector error, amplitude error, and phase lag error for M_2 and S_2 than the other models, and its performance for the remaining constituents is among the best. However, for the Q_1 constituent, the ENOPF dataset only outperforms the EOT20 model.

As demonstrated in this study, the cotidal charts derived from the dataset exhibit smooth, continuous isophase lines and a well-organized distribution of amphidromic points, which is notably superior to the fragmented isophase lines observed in the EOT20 model. Nevertheless, all models show overall consistency in the spatial distribution of tidal constituent amplitudes and the geographical positions of amphidromic points. It is worth noting that, based on the 3′×3′ resolution dataset used in this study, the corresponding polynomial coefficients can be directly extracted to construct a high-precision 1′×1′ grid of tidal harmonic constants. The dataset has been proven to be reliable and of high quality for evaluating tidal harmonics in the Central Pacific Basin. This high-precision tidal harmonics dataset for the Central Pacific Basin offers significant application advantages, providing more reliable data support and technical references for tidal dynamics, ocean circulation, and marine engineering projects in the region.

Data availability

Data are available in Zenodo (DOI: https://doi.org/10.5281/zenodo.19905533, Meng et al., 2026) and will be made open access upon publication. Reviewers can access the data anonymously via the review link: https://zenodo.org/records/19905533?token=eyJhbGciOiJIUzUxMiIsImlhdCI6MTc3NzUzNDE0NywiZXhwIjoxODA1OTMyNzk5fQ.eyJpZCI6ImQ4ODQzODYzLTg3Y2EtNDA0MS1iZWU5LTM3NmFhMjFiZjEwYyIsImRhdGEiOnt9LCJyYW5kb20iOiI3YWQwZDM4NmQ1NmJmZjM0N2Y5ZmM5OTAxZjJlZDk1OCJ9.ytQuDIzjSmz8LpHRt2293MmOcHDjj2lz5V-XZDJfZ1J1BpxMFMs1GywmecBkyvjnZP92o6kff-fk2BpsBI3sqg.

https://doi.org/10.5194/essd-2026-233
Preprint. Discussion started: 8 May 2026

Author contributions

Deyu Meng authored the paper, Xianqing Lv and Xiaojiang Zhang provided the methodology, Yunfei Zhang and Yibo Zhang provided the data and verified the comparison results between satellite altimeters and tide gauges. There are no competing interests among the authors. All authors read, commented and reviewed the final manuscript.

Competing interests

The authors declare that they have no conflict of interest.

Disclaimer

Copernicus Publications adds a standard disclaimer: "Copernicus Publications remains neutral with regard to jurisdictional claims made in the text, published maps, institutional affiliations, or any other geographical representation in this paper. While Copernicus Publications makes every effort to include appropriate place names, the final responsibility lies with the authors. Views expressed in the text are those of the authors and do not necessarily reflect the views of the publisher."
Please feel free to add disclaimer text at your choice, if applicable.

Acknowledgements

The authors thank T/P- Jason satellite altimeter data, tide gauge data from the University of Hawaii Sea Level Center (UHSLC) and FES2014, FES2022b, EOT20, TPXO10, and DTU16. The T/P altimeter data are provided by the National Aeronautics and Space Administration (NASA) (http://marine.copernicus.eu/services-portfolio/access-to-products/), Jason-1 data can be downloaded from http://podaac.jpl.nasa.gov , Jason-2 data can be downloaded from http://www.class.noaa.gov , andJason-3 data can be downloaded from http://www.class.noaa.gov/saa/products/user_profile . Tide gauge data can be downloaded from https://uhslc.soest.hawaii.edu/. FES2014 and FES2022b can be downloaded from https://www.aviso.altimetry.fr/ . EOT20 can be downloaded from https://doi.org/10.17882/79489 . TPXO10 can be downloaded from https://www.tpxo.net/global/tpxo10-atlas. DTU16 can be downloaded from ftp://ftp.space.dtu.dk/pub/DTU16/OCEAN_TIDE/ .

Financial support

This research was funded by the Self-Initiated Research of Naval Aviation University, the National Natural Science Foundation of China (Grant No. 42506024), the National Key Research and Development Program of China (Grant No.2022YFC3105003) and the National Natural Science Foundation of China (Grant No. 42076011 and Grant No. U2006210).

https://doi.org/10.5194/essd-2026-233
Preprint. Discussion started: 8 May 2026

Review statement

The review statement will be added by Copernicus Publications listing the handling editor as well as all contributing referees according to their status anonymous or identified.

References

Cheng, Y. and Andersen, O. B.: Multimission empirical ocean tide modeling for shallow waters and polar seas, Journal of Geophysical Research: Oceans, 116, https://doi.org/10.1029/2011JC007172, 2011.

Doodson, A. T.: Perturbations of harmonic tidal constants, Proceedings of the Royal Society of London. Series a, Containing Papers of a Mathematical and Physical Character, 106, 513-526, https://doi.org/10.1098/rspa.1924.0085, 1924.

Egbert, G. D. and Erofeeva, S. Y.: Efficient inverse modeling of barotropic ocean tides, J. Atmos. Ocean. Technol., 19, 183-204, https://doi.org/10.1175/1520-0426(2002)019<0183:eimobo>2.0.co;2, 2002.

Eisinberg, A. and Fedele, G.: Discrete orthogonal polynomials on equidistant nodes, International Mathematical Forum, 2, 1007-1020, https://doi.org/10.12988/imf.2007.07087, 2007.

Fang, G., Wang, Y., Wei, Z., Choi, B. H., Wang, X., and Wang, J.: Empirical cotidal charts of the bohai, yellow, and east china seas from 10 years of TOPEX/poseidon altimetry, Journal of Geophysical Research: Oceans, 109, https://doi.org/10.1029/2004JC002484, 2004.

Foreman, M. G. G. and Henry, R. F.: The harmonic analysis of tidal model time series, Adv. Water Resour., 12, 109-120, https://doi.org/10.1016/0309-1708(89)90017-1, 1989.

Fu, Y., Wang, P., Peng, F., Feng, Y., Khaki, M., and Mi, X.: Accurate extraction of ocean tidal constituents from coastal satellite altimeter records, Front. Mar. Sci., 12, https://doi.org/10.3389/fmars.2025.1592765, 2025.

Green, J. A. M., Green, C. L., Bigg, G. R., Rippeth, T. P., Scourse, J. D., and Uehara, K.: Tidal mixing and the meridional overturning circulation from the last glacial maximum, Geophys. Res. Lett., 36, https://doi.org/10.1029/2009GL039309, 2009.

Hart-Davis, M. G., Dettmering, D., Sulzbach, R., Thomas, M., Schwatke, C., and Seitz, F.: Regional evaluation of minor tidal constituents for improved estimation of ocean tides, Remote Sens., 13, 3310, https://doi.org/10.3390/rs13163310, 2021.

Hart-Davis, M. G., Piccioni, G., Dettmering, D., Schwatke, C., Passaro, M., and Seitz, F.: EOT20: a global ocean tide model from multi-mission satellite altimetry, Earth Syst. Sci. Data, 13, 3869-3884, https://doi.org/10.5194/essd-13-3869-2021, 2021.

Hu, J., Gurnis, M., Rudi, J., Stadler, G., and Müller, R. D.: Dynamics of the abrupt change in pacific plate motion around 50 million years ago, Nat. Geosci., 15, 74-78, https://doi.org/10.1038/s41561-021-00862-6, 2022.

Idier, D., Bertin, X., Thompson, P., and Pickering, M. D.: Interactions between mean sea level, tide, surge, waves and flooding: mechanisms and contributions to sea level variations at the coast, Surv. Geophys., 40, 1603-1630, https://doi.org/10.1007/s10712-019-09549-5, 2019.

https://doi.org/10.5194/essd-2026-233
Preprint. Discussion started: 8 May 2026

Kawasaki, T., Hasumi, H., and Tanaka, Y.: Role of tide-induced vertical mixing in the deep pacific ocean circulation, J. Oceanogr., 77, 173-184, https://doi.org/10.1007/s10872-020-00584-0, 2021.

Luneva, M. V., Aksenov, Y., Harle, J. D., and Holt, J. T.: The effects of tides on the water mass mixing and sea ice in the arctic ocean, J. Geophys. Res. Oceans, 120, 6669-6699, https://doi.org/10.1002/2014JC010310, 2015.

Luther, D. S. and Wunsch, C.: Tidal charts of the central pacific ocean, J. Phys. Oceanogr., 5, 222-230, 1975.

Lyard, F. H., Allain, D. J., Cancet, M., Carr Ere, L., and Picot, N.: FES2014 global ocean tide atlas: design and performance, Ocean Sci., 17, 615-649, https://doi.org/10.5194/os-17-615-2021, 2021.

Meng, D., Zhang, Y., Zhang, Y., Lv, X., and Zhang, X.: Eight major tidal constituents from the ENOPF method in the central Pacific, Zenodo [data set], https://doi.org/10.5281/zenodo.19905533, 2026.

Mofjeld, H. O.: Tides, surges and mean sea-level, a handbook for engineers and scientists, Eos, Transactions American Geophysical Union, 69, 850, https://doi.org/10.1029/88EO01109, 1988.

Munk, W.: Once again: once again—tidal friction, Prog. Oceanogr., 40, 7-35, https://doi.org/10.1016/S0079-6611(97)00021-9, 1997.

Niwa, Y. and Hibiya, T.: Numerical study of the spatial distribution of the m2 internal tide in the pacific ocean, Journal of Geophysical Research: Oceans, 106, 22441-22449, https://doi.org/10.1029/2000JC000770, 2001.

Parianos, J. and Madureira, P.: Geomorphology of the clarion clipperton zone, tropical north pacific ocean, J. Maps, 17, 760-768, https://doi.org/10.1080/17445647.2021.2001387, 2021.

Pawlowicz, R., Beardsley, B., and Lentz, S.: Classical tidal harmonic analysis including error estimates in MATLAB using t_TIDE, Comput. Geosci., 28, 929-937, https://doi.org/10.1016/S0098-3004(02)00013-4, 2002.

Ray, R. D. and Cartwright, D. E.: Estimates of internal tide energy fluxes from topex/poseidon altimetry: central north pacific, Geophys. Res. Lett., 28, 1259-1262, https://doi.org/https://doi.org/10.1029/2000GL012447, 2001.

Seifi, F., Deng, X., and Andersen, O. B.: Assessment of the accuracy of recent empirical and assimilated tidal models for the great barrier reef, australia, using satellite and coastal data, Remote Sens., 11, 1211, https://doi.org/10.3390/rs11101211, 2019.

Stammer, D., Ray, R. D., Andersen, O. B., Arbic, B. K., Bosch, W., Carrère, L., Cheng, Y., Chinn, D. S., Dushaw, B. D., Egbert, G. D., Erofeeva, S. Y., Fok, H. S., Green, J. A. M., Griffiths, S., King, M. A., Lapin, V., Lemoine, F. G., Luthcke, S. B., Lyard, F., Morison, J., Müller, M., Padman, L., Richman, J. G., Shriver, J. F., Shum, C. K., Taguchi, E., and Yi, Y.: Accuracy assessment of global barotropic ocean tide models, Rev. Geophys., 52, 243-282, https://doi.org/10.1002/2014rg000450, 2014.

Talke, S. A. and Jay, D. A.: Changing tides: the role of natural and anthropogenic factors, Annu. Rev. Mar. Sci., 12, 121-151, https://doi.org/10.1146/annurev-marine-010419-010727, 2020.

Wang, Y., Zhang, Y., Xu, M., Wang, Y., and Lv, X.: Ocean tides near hawaii from satellite altimeter data. Part II, J. Atmos. Ocean. Technol., 39, 1015-1029, https://doi.org/10.1175/jtech-d-21-0087.1, 2022.

Weber, T. and Thomas, M.: Tidal dynamics and their influence on the climate system from the cretaceous to present day,

Glob. Planet. Change, 158, 173-183, https://doi.org/10.1016/j.gloplacha.2017.09.019, 2017.

Xu, M., Wang, Y., Wang, S., Lv, X., and Chen, X.: Ocean tides near hawaii from satellite altimeter data. Part i, J. Atmos. Ocean. Technol., 38, 937-949, https://doi.org/10.1175/jtech-d-20-0072.1, 2021.

Yanagi, T., Morimoto, A., and Ichikawa, K.: Co-tidal and co-range charts for the east china sea and the yellow sea derived from satellite altimetric data, Oceanographic Literature Review, 1997.

Zetler, B. D., Schuldt, M. D., Whipple, R. W., and Hicks, S. D.: Harmonic analysis of tides from data randomly spaced in time, Journal of Geophysical Research (1896-1977), 70, 2805-2811, https://doi.org/10.1029/JZ070i012p02805, 1965.

Zhang, Y., Jiao, S., Jiang, D., and Lv, X.: Estimating ocean tides in the south china sea by assimilating satellite data using 2d tidal adjoint model and equidistant nodes orthogonal polynomial fitting, J. Atmos. Ocean. Technol., https://doi.org/10.1175/jtech-d-24-0101.1, 2025.

Zhang, Y., Jiao, S., Wang, Y., Wang, Y., and Lv, X.: Ocean tides near hawaii from satellite altimeter data. Part III, J. Atmos. Ocean. Technol., 40, 491-501, https://doi.org/10.1175/jtech-d-22-0052.1, 2023.

Zhang, Y., Kong, C., Liu, Z., Li, B., and Lv, X.: Assessing tidal models in the ryukyu islands region using the ENOPF method, J. Atmos. Ocean. Technol., https://doi.org/10.1175/jtech-d-23-0101.1, 2024.

Zhang, Y., Wang, Q., Zhang, Y., Xu, M., Wang, Y., and Lv, X.: Equidistant nodes orthogonal polynomial fitting for harmonic constants of long-period tides based on satellite altimeter data, Remote Sens., 15, 3246, https://doi.org/10.3390/rs15133246, 2023.

Zhang, Y., Zhang, X., Ren, K., Wang, H., Zhang, W., and Lv, X.: High-resolution tidal harmonic reconstruction in the south china sea using ENOPF and a 2d adjoint tidal model, Cont. Shelf Res., 105645, https://doi.org/10.1016/j.csr.2026.105645, 2026.